Research Square

Preprints are preliminary reports that have not undergone peer review.
They should not be considered conclusive, used to inform clinical practice,
or referenced by the media as validated information.

Integrated Microcomb-Driven Vortex Electromagnetic Waves for Broadband Forward-looking Sensing

Jijun He

jijun.he@nuaa.edu.cn

Nanjing University of Aeronautics and Astronautics https://orcid.org/0000-0001-7011-4386

Guanqun Sun

Nanjing Normal University

Zhekai Zheng

Nanjing University of Aeronautics and Astronautics

Jiacheng Guo

Nanjing University of Aeronautics and Astronautics

Wenjun Qi

Hohai University

Ding Cui

Nanjing University of Aeronautics and Astronautics

Hao Zhang

Max Planck Institute for the Science of Light https://orcid.org/0000-0001-7497-480X

Fangzheng Zhang

Nanjing University of Aeronautics and Astronautics

Yiping Wang

Nanjing Normal University https://orcid.org/0000-0001-7366-6426

Shilong Pan

Nanjing University of Aeronautics and Astronautics https://orcid.org/0000-0003-2620-7272

Article

Keywords:

Posted Date: March 24th, 2026

DOI: https://doi.org/10.21203/rs.3.rs-9112621/v1

License: This work is licensed under a Creative Commons Attribution 4.0 International License.
Read Full License

Additional Declarations: There is **NO** Competing Interest.

Integrated Microcomb-Driven Vortex Electromagnetic Waves for Broadband Forward-looking Sensing

Guanqun Sun[1†], Zhekai Zheng[2†], Jiacheng Guo[2], Wenjun Qi[3], Ding Cui[2], Hao Zhang[2*], Jijun He[2*], Fangzheng Zhang[2*], Yiping Wang[1*], Shilong Pan[2*]

[1*]School of Computer and Electronic Information, Nanjing Normal University, Nanjing, 210023, China.

[2]National Key Laboratory of Microwave Photonics, Nanjing University of Aeronautics and Astronautics, Nanjing 210016, China.

[3]College of Information Science and Engineering, Hohai University, Nanjing 210024, China.

*Corresponding author(s). E-mail(s): jamzhang627@gmail.com; jijun.he@nuaa.edu.cn; zhangfangzheng@nuaa.edu.cn; ypwang@njnu.edu.cn; pans@nuaa.edu.cn;
Contributing authors: sunguanqun@nnu.edu.cn; zhengzk@nuaa.edu.cn; guojc452@nuaa.edu.cn; qiwenjun@hhu.edu.cn; cdjinge@nuaa.edu.cn;
†These authors contributed equally to this work.

Abstract

Microwave sensing is a critical enabler for all-weather perception, yet its resolution is severely limited when relative motion or large effective apertures are unavailable. Vortex electromagnetic (EM) waves can provide additional azimuthal discrimination, but practical deployment is constrained by the trade-off between bandwidth, mode purity, and hardware complexity. Here, we propose a microwave photonic architecture enabled by a chip-scale dissipative Kerr soliton microcomb that resolves these constraints. The microcomb provides more than 100 optical lines with linewidths below 30 kHz. By optically processing these carriers, we synthesize vortex waves covering an 8 GHz bandwidth (18–26 GHz) with 15 programmable orbital angular momentum (OAM) modes. Compared with a conventional implementations, our approach exhibits higher OAM purity and improved field integrity across the band, while condensing the multi-wavelength source onto a monolithic chip. We demonstrate superior forward-looking imaging performance, clearly resolving both point targets and complex scenes. This work bridges integrated soliton physics with broadband microwave processing, establishing a scalable framework for next-generation compact, high-performance smart sensors.

Introduction

Microwave sensing constitutes a cornerstone of modern perception technology, underpinning critical applications ranging from autonomous navigation and remote surveillance to non-destructive evaluation and environmental monitoring [1–3]. Despite notable progress, most systems remain fundamentally constrained by the range–Doppler paradigm [4–6]. In this regime, range resolution is dictated by the signal bandwidth, while azimuth resolution relies on the synthetic aperture formed by relative motion between the radar and the target. Crucially, in forward-looking scenarios where such motion is absent or restricted, the small effective aperture would result in poor azimuth discrimination. Although single-pulse [7] and deconvolution [8] techniques offer partial improvements, they remain bounded by physical antenna limits and electronic bandwidths. These limitations hinder further development in microwave sensing, necessitating new sensing theories and system architectures.

Wavefront modulation provides a complementary route to sensing beyond conventional degrees of freedom in time, frequency and polarization. In particular, vortex electromagnetic (EM) waves carrying orbital angular momentum (OAM) exhibit helical phase fronts, causing targets under such illumination to exhibit spatially structured, mode-dependent scattering [9–12]. The mutual orthogonality of OAM eigenmodes expands the sensing space and enriches echo information, enabling finer discrimination without relative motion. These properties have catalyzed sustained

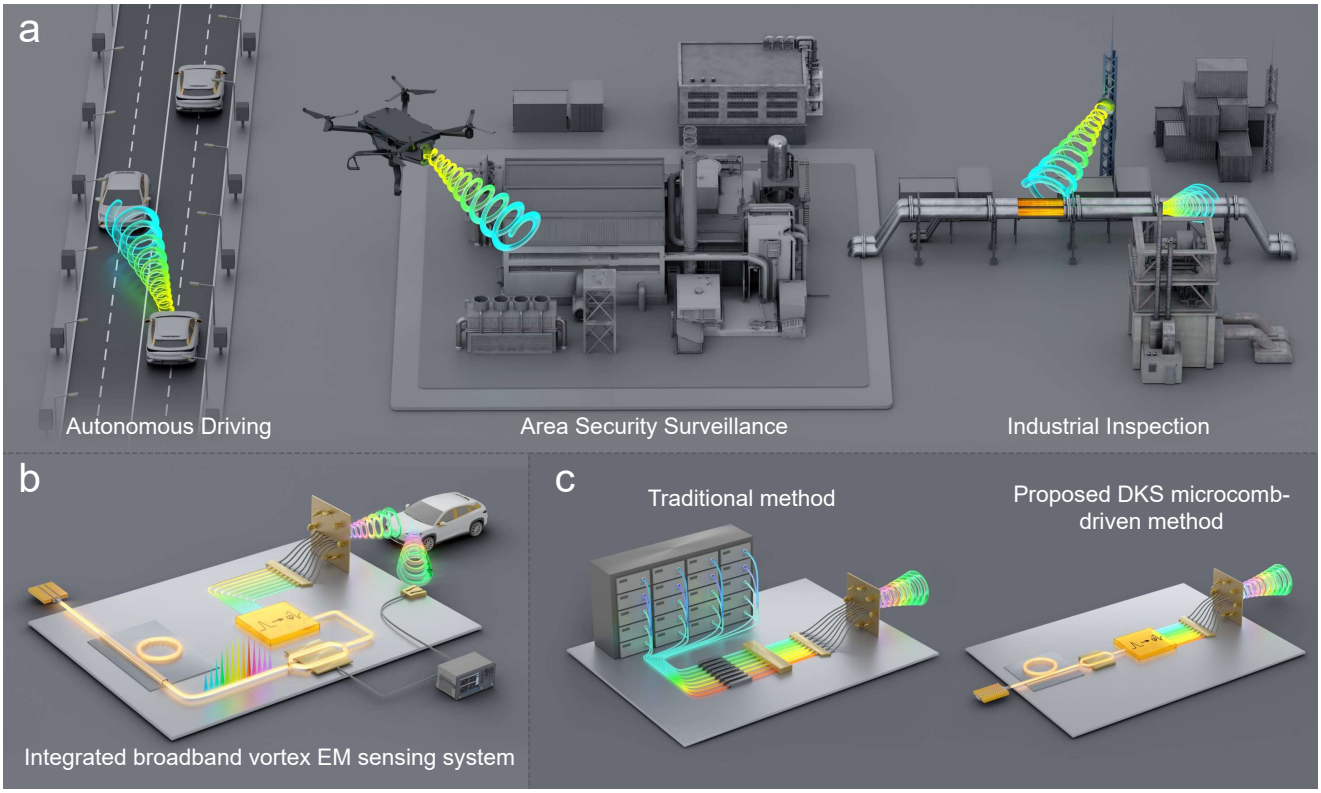


Figure 1. **Integrated broadband vortex EM sensing system. a.** Envisioned application scenarios of the integrated broadband vortex EM sensing system, including autonomous driving, area security surveillance, and industrial inspection systems. **b.** Schematic illustration of the integrated broadband vortex EM sensing system. A microcomb-based source feeds the optical signal-processing for broadband vortex EM wave synthesis, followed by transmission and echo acquisition. **c.** Conceptual comparison between a free-running parallel-laser implementation and the proposed microcomb-driven implementation.

interest in vortex EM sensing technology, including generation of vortex EM fields, high-resolution vortex-based imaging, and efficient detection of rotational Doppler shifts [13–18].

However, realizing this potential faces a critical bottleneck involving the trade-off between signal bandwidth for range resolution and mode density for azimuth resolution. Recent photonic-based approaches have demonstrated broadband vortex EM waves generation [19, 20], but scaling the azimuth resolving power by increasing the OAM mode count typically relies on multiple lasers at distinct wavelengths. In such free-running parallel-laser configurations, independent phase drifts and linewidth-induced fluctuations degrade the designed inter-channel phase relationship, which in turn reduces OAM purity and introduces mode aliasing. Although an array of costly ultra-narrow-linewidth lasers with complex active phase-locking loops can partly alleviate this issue, it substantially increases hardware complexity and limits scalability.

Photonic integrated circuits (PICs) provide a promising route toward compact, energy-efficient, and scalable sources essential for next-generation sensing [21–24]. However, existing approaches still face difficult trade-offs between linewidth, power, bandwidth, and complexity [25]. For instance, chip-scale arrays like self-injection-locked distributed-feedback (DFB) lasers often suffer from broad linewidths (typically exceed hundreds of kilohertz). Although heterogeneous integration with ultrahigh-Q microresonators can reduce the linewidth [26, 27], scaling such architectures to hundreds of channels introduces substantial challenges in fabrication uniformity, multi-channel locking control, and overall chip footprint. Electro-optic frequency combs offer an alternative route with intrinsically uniform comb-line linewidths and flat power distribution. However, cascaded-modulation combs are generally limited to a few nanometers of optical bandwidth and rely on external complex microwave driving systems[28–31]. These constraints hinder their use in large-scale, multi-wavelength integrated systems that demand both broad bandwidth and consistent coherence.

Kerr microcombs, generated in dispersion-engineered microresonators through third-order nonlinearity, have recently emerged as a compelling solution to these bottlenecks. Driven into the dissipative Kerr soliton (DKS) regime, they naturally provide broadband spectra spanning hundreds of nanometers with a smooth $sech^2$ envelope and tens-of-nanometers 3-dB bandwidths[32]. Crucially, when driven by a narrow-linewidth pump, the central comb lines, typically numbering over 100 near the pump frequency, inherit the pump's high phase coherence. While thermo-refractive noise (TRN) would affect distant comb lines

[33–36], it is well-established that the lines proximate to the pump maintain exceptional stability [34, 37], and residual noise can be further mitigated through auxiliary laser cooling [38] or cavity dispersion engineering [39]. These attributes make Kerr microcombs a compelling source technology for scalable multi-channel coherent microwave photonic systems.

In this work, we propose an integrated microcomb-driven architecture that synthesizes high-purity, broadband vortex EM waves for high-performance microwave sensing. By driving a high-Q microcavity into the DKS regime, our system replaces bulky discrete laser arrays, providing a dense spectrum of highly stable optical carriers. The ultra-narrow linewidth and intrinsic mutual coherence of the integrated comb source effectively eliminate the stochastic phase jitter typical of parallel-laser configurations, ensuring superior inter-channel coherence. Powered by this microcomb, an integrated Mach–Zehnder modulator (MZM) maps a broadband frequency-swept signal onto the carriers, which are then manipulated by a programmable optical signal processor to apply required channel-dependent phase shifts. This optical-domain processing maintains an inherently flat frequency response, minimizing intra-channel variations across the entire wideband operation.

Using this architecture, we experimentally realize a 16-channel vortex EM sensing system operating across the K-band (18–26 GHz), supporting an 8 GHz bandwidth and 15 programmable OAM modes (l = 0, ±1, ..., ±7). Through field characterization and forward-looking imaging experiments, we show that the microcomb-driven implementation provides improved field integrity and higher OAM-mode purity than conventional electronic or parallel-laser approaches. These advantages translate into clearer target reconstruction for both isolated point targets and complex scenes, demonstrating strong potential for high-performance target detection and imaging. By combining photonic integrated circuits with broadband microwave photonic signal processing, this work establishes a general chip-scale platform for motion-free sensing enhancement. The framework is readily extendable to larger mode counts, reconfigurable beamforming, and joint communications-sensing functions, opening opportunities in autonomous driving, area security surveillance, and industrial inspection where compact and stable high-performance sensing is paramount (as shown in Figure.1 a).

Results

Integrated broadband vortex EM sensing system architecture

The proposed integrated broadband vortex EM sensing system, schematically illustrated in Figure. 1b, consists of three functional modules: an integrated broadband signal generator, a broadband signal-processing unit, and a vortex EM transceiver. The first module serves as the coherent source. Instead of using banks of discrete, uncorrelated lasers, we use a high-Q microcavity resonator driven into the DKS regime. This microcomb provides a dense spectrum of stable, spectrally clean lines derived from a single narrow-linewidth pump. These lines serve as carriers for an integrated MZM, onto which a broadband frequency-swept RF signal is multicast to form parallel RF channels. The optical signal-processing unit then employs a programmable optical waveshaper to demultiplex the channels and applies the phase profiles required for vortex EM wave synthesis. Finally, the phase-coded signals are radiated by a uniform circular array (UCA) to generate broadband vortex EM waves, and echoes are captured by a single receiving antenna for digital reconstruction.

As illustrated in Figure. 1c, our architecture fundamentally addresses the bottlenecks of current vortex EM sensing. First, the DKS microcomb replaces bulky discrete laser banks, reducing system footprint, cost and complexity. Furthermore, its dense optical spectrum increases the usable channel count. This directly extends the set of accessible OAM modes without additional hardware. More importantly, the comb lines inherit the narrow linewidth and stability of the master pump, yielding measurably superior inter-channel coherence compared to free-running parallel-laser sources. Second, processing in the optical domain treats the RF waveform as a small fractional bandwidth relative to the optical carrier. This enables precise amplitude-phase weighting with a much flatter broadband response than electronic phase shifters and attenuators. Collectively, these advantages facilitate the generation of high-quality, multi-mode broadband vortex EM waves using a more compact system, enabling high-performance microwave sensing.

Integrated multi-channel broadband signal generation and control

We implemented the source module using a narrow-linewidth continuous-wave laser (NKT Koheras ADJUSTIK E15) at 1550.13 nm as the pump. The pump light was amplified to 26 dBm by an erbium-doped fiber amplifier (EDFA, CONNET MFAS-EY-C-B) and passed through an optical bandpass filter to suppress amplified spontaneous emission (ASE) noise. The Si_3N_4 chip used in this work was fabricated by Qaleido Photonics [40]. The dispersion and free spectral range (FSR) of the anomalous-dispersion Si_3N_4 micro-ring resonator were both characterized using our home-built optical vector analysis (OVA) system [41]. The purified light was then coupled into the Si_3N_4 micro-ring resonator chip via a lensed fiber [42], as illustrated in Figure. 2 (detailed device characterization is provided in Supplementary Note 1). The MRR temperature was strictly stabilized at 20 ± 0.1 °C using a thermoelectric cooler (TEC).

By applying a precise combination of forward and backward tuning techniques [43–45], we successfully generated single-soliton microcombs. After suppressing

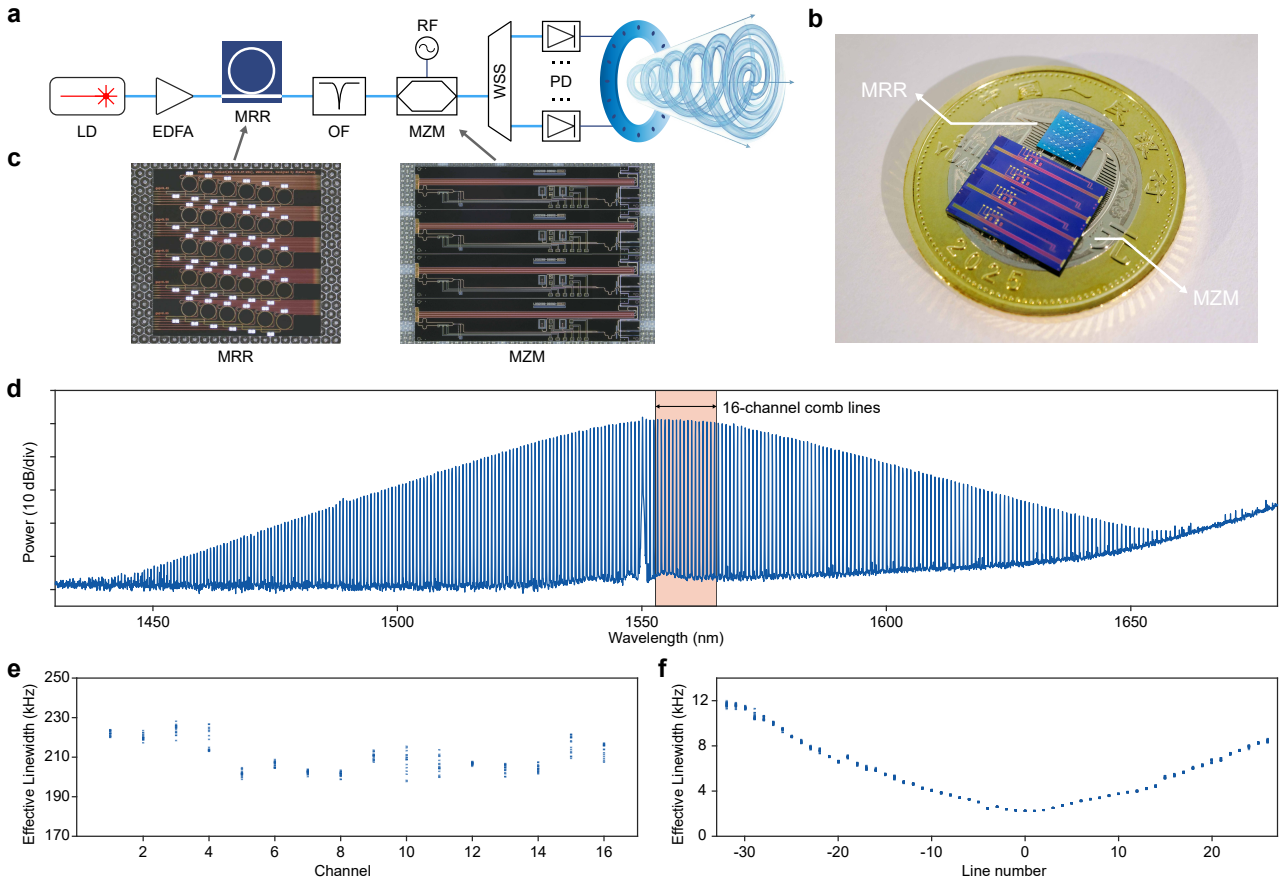


Figure 2. **Integrated microcomb-driven vortex electromagnetic wave source. a.** Schematic of the proposed device. LD, laser diode; EDFA, erbium-doped fiber amplifier; MRR, microring resonator; OF, optical filter; MZM, Mach-Zehnder modulator; RF, radio-frequency source; WSS, programmable waveshaper; PD, photodetector. **b.** Optical micrograph of the fabricated chip. **c.** Magnified microscope images of the MRR and MZM regions. **d.** Optical spectrum of the generated Kerr frequency comb. **e. f.** Effective linewidth measurements of the 16 individual reference lasers (e) and the generated Kerr microcomb (f).

the strong pump component with a tunable fiber Bragg grating (FBG), the optical spectrum was recorded using an optical spectrum analyzer (DEVISER AE8700). As shown in Figure. 2d, the measured soliton microcomb exhibits a characteristic $sech^2$ spectral envelope extending over more than 200 nm, containing over 270 comb lines with a 3-dB bandwidth exceeding 32 nm. The effective linewidths of the Kerr comb lines were characterized using the non-zero-frequency delayed self-heterodyne method, and compared with those of a reference benchtop laser (Figure. 2e and Figure. 2f). Due to TRN, the measured linewidths exhibit a parabolic dependence centered at the pumped resonance. Limited by the operational bandwidth of the C-band small-signal optical amplifier (Amonics AEDFA-PA-35-B-FA) used to boost individual lines for measurement, we characterized 59 comb lines spanning indices μ = -32 to μ = +26. The farthest measured line exhibited an effective linewidth below 12 kHz. Based on this distribution, it is expected that more than one hundred comb lines maintain effective linewidths below 30 kHz. Furthermore, this linewidth performance could be further improved by suppressing TRN through auxiliary laser cooling or cavity dispersion engineering [38, 39].

To generate multi-channel broadband RF signals, the soliton microcomb was amplified and fed into an integrated MZM. This MZM was driven by a vector network analyzer (VNA, Agilent N5235A) performing a linear frequency sweep from 18 to 26 GHz with a step size of 0.2 MHz. By properly biasing the MZM, $\pm 1^{st}$ order modulation sidebands corresponding to the input RF signal were multicast onto the coherent optical carriers, establishing parallel probing channels. Subsequently, a programmable optical signal processor (Waveshaper 16000A) was employed to slice and manipulate the spectrum. While a discrete component is used here for experimental flexibility, this functionality is compatible with emerging on-chip beamforming networks. We selected $N = 16$ specific channels from the modulated DKS comb to serve as the OAM emitters. Beyond simple filtering, the processor applied channel-specific attenuation for spectral equalization and imprinted the requisite phase shifts defined by $\varphi_n = 2\pi ln/N$ between the n^{th} optical carrier and its $\pm 1^{st}$ order modulation sideband. This optical-domain processing ensures precise wavefront synthesis after the signals are converted back to the electrical domain for radiation. The phase-coded optical signals were converted into the electrical

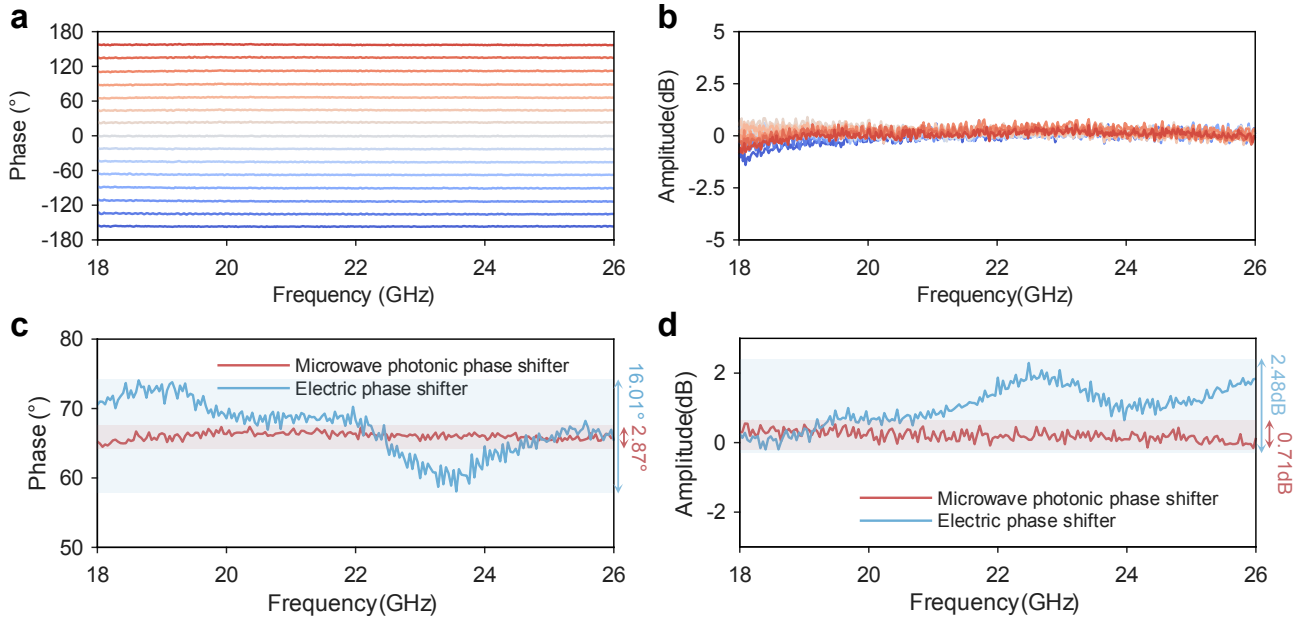


Figure 3. **Properties of microwave photonic signal processor. a.** Measured phase responses from 18 to 26 GHz for programmed offsets corresponding to OAM modes l = -7 to +7 (steps of 22.5°). **b.** Measured amplitude responses corresponding to the phase states in a, showing minimal frequency-dependent variation. **c. d.** Comparative measurement of a commercial electronic phase shifter under the same 67.5° phase setting. The photonic approach exhibits smaller phase and amplitude variations across the band (2.87° and 0.71 dB, respectively) than the electronic device (16.01° and 0.71 dB, respectively).

domain using an array of high-speed photodetectors (u2t XPDV2120RA, 40 GHz bandwidth). The resulting RF signals were radiated by a UCA comprising 16 K-band horn antennas (18–26.5 GHz) arranged with a radius of 8.18 cm (approximately six times the center wavelength). A single K-band horn antenna positioned at the array center served as the receiver to acquire echoes for digital processing.

We quantitatively characterized the performance of the microwave photonic signal-processing mechanism using the first channel (λ_1 = 1553.21 nm) as a representative test case (Figure. 3). By adjusting the optical phase difference between the carrier and the sideband, the RF phase was continuously tuned from -180° to 180°. Figure. 3a displays the measured phase responses for the discrete offsets (-157.5°, -135°, -112.5°, -90°, -67.5°, -45°, -22.5°, 0°, 22.5°, 45°, 67.5°, 90°, 112.5°, 135°, and 157.5°) required to generate OAM modes ranging from l = -7 to +7. The phase response remains essentially flat across the full 18–26 GHz sweep. Correspondingly, the amplitude response (Figure. 3b) exhibits small variation with frequency, with the maximum fluctuation limited to 2.31 dB.

For comparison, we measured a commercial digital phase shifter (Talent Microwave TLDP-18G26.5G-6) under the same nominal phase setting (Figure. 3c, d). The photonic approach demonstrates superior broadband stability, with maximum variations limited to 2.87° in phase and 0.71 dB in amplitude across the band. In contrast, the electronic unit exhibits significant frequency-dependent fluctuations, with maximum deviations reaching 16.01° and 2.48 dB, respectively. This superior smoothness minimizes intra-channel dispersion, ensuring waveform integrity across the wide operation bandwidth. Collectively, the constructed compact system generates multi-channel broadband RF signals with independently adjustable phases and low inter- and intra-channel errors, providing a robust foundation for high-performance vortex EM sensing applications.

Vortex electromagnetic field observation and analysis

We conducted equivalent field observations in an anechoic chamber to comprehensively assess the radiation characteristics of the generated vortex EM waves. The observation window (1 m × 1 m) was positioned 3 m away from the UCA plane to capture the cross-sectional field distributions. The experimental testbed and measurement environment are detailed in Supplementary Note 2. For the microcomb-driven system, the measured fields exhibit excellent agreement with theoretical predictions across the full operation bandwidth. As shown in Figure. 4a, the phase distributions display clear, continuous helical wavefronts with phase changes of $2\pi l$ around the singularity, corresponding to OAM modes l = 1, 3, 5, 7 at frequencies of 18, 22, and 26 GHz. Concurrently, the intensity distributions feature the characteristic ring-shaped profiles with a deep central null and uniform annular energy distribution. These observations confirm that the integrated platform successfully synthesizes broadband vortex EM fields with high structural integrity.

To examine the role of source coherence, we performed a baseline comparison using a conventional

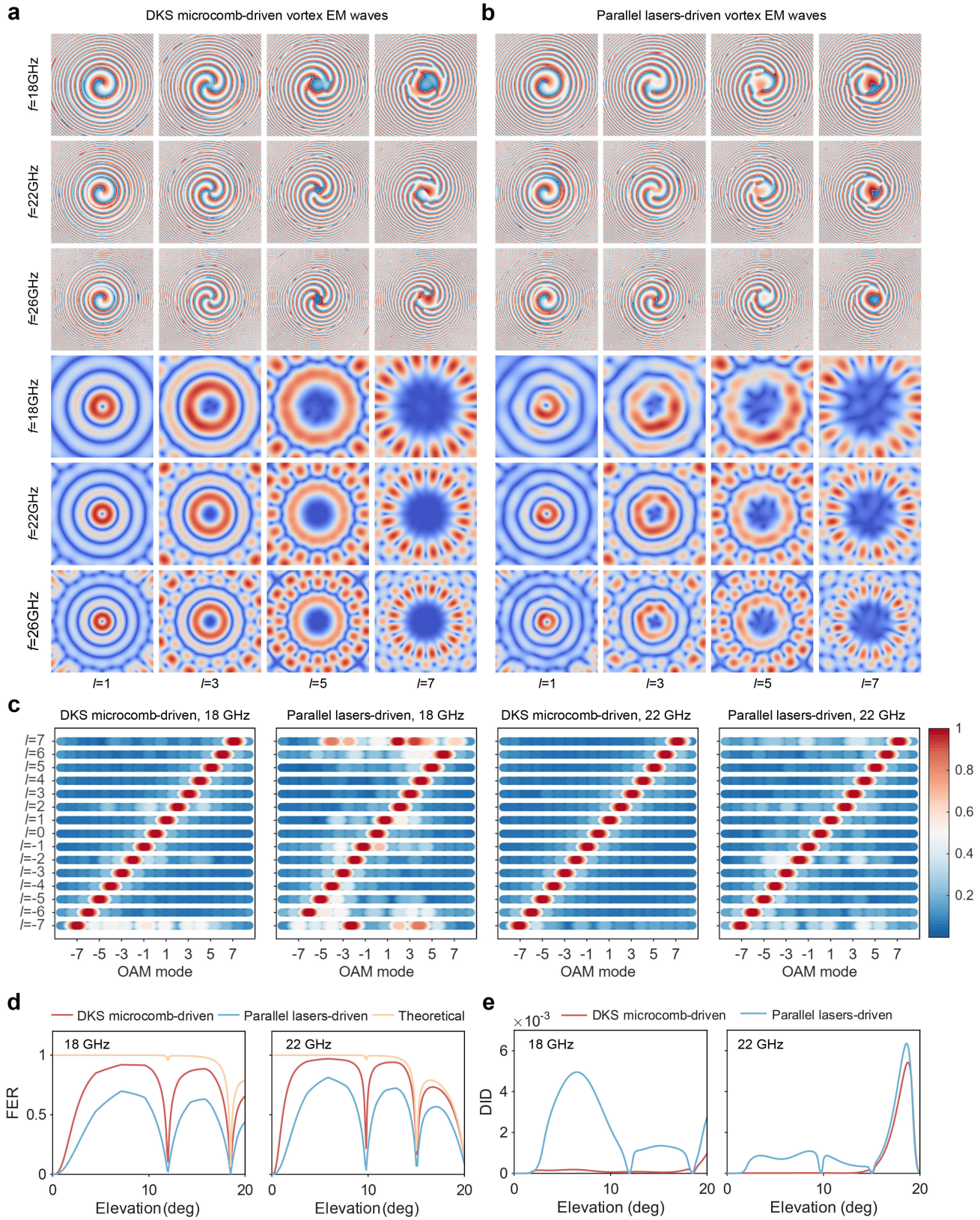


Figure 4. **Field characterization and mode-purity analysis of the generated vortex EM waves. a.** Measured phase (top three rows) and amplitude (bottom three rows) patterns for the microcomb-driven system at 18, 22, and 26 GHz for OAM modes $l = 1, 3, 5, 7$, showing clear helical wavefronts and ring-shaped intensity profiles. **b.** Comparative field measurements for the parallel laser-driven baseline under the same conditions. The fields exhibit significant distortion and indistinct phase singularities. **c.** OAM spectral decomposition for microcomb-driven and parallel laser-driven systems under different OAM mode (l = -7 to 7) at 18 GHz and 22 GHz (elevation 8°). **d. e.** Quantitative evaluation of mode purity using the Fundamental-mode Energy Ratio (FER, d) and Degree of Intensity Deviation (DID, e) for $l = 3$ at 18 GHz and 22 GHz.

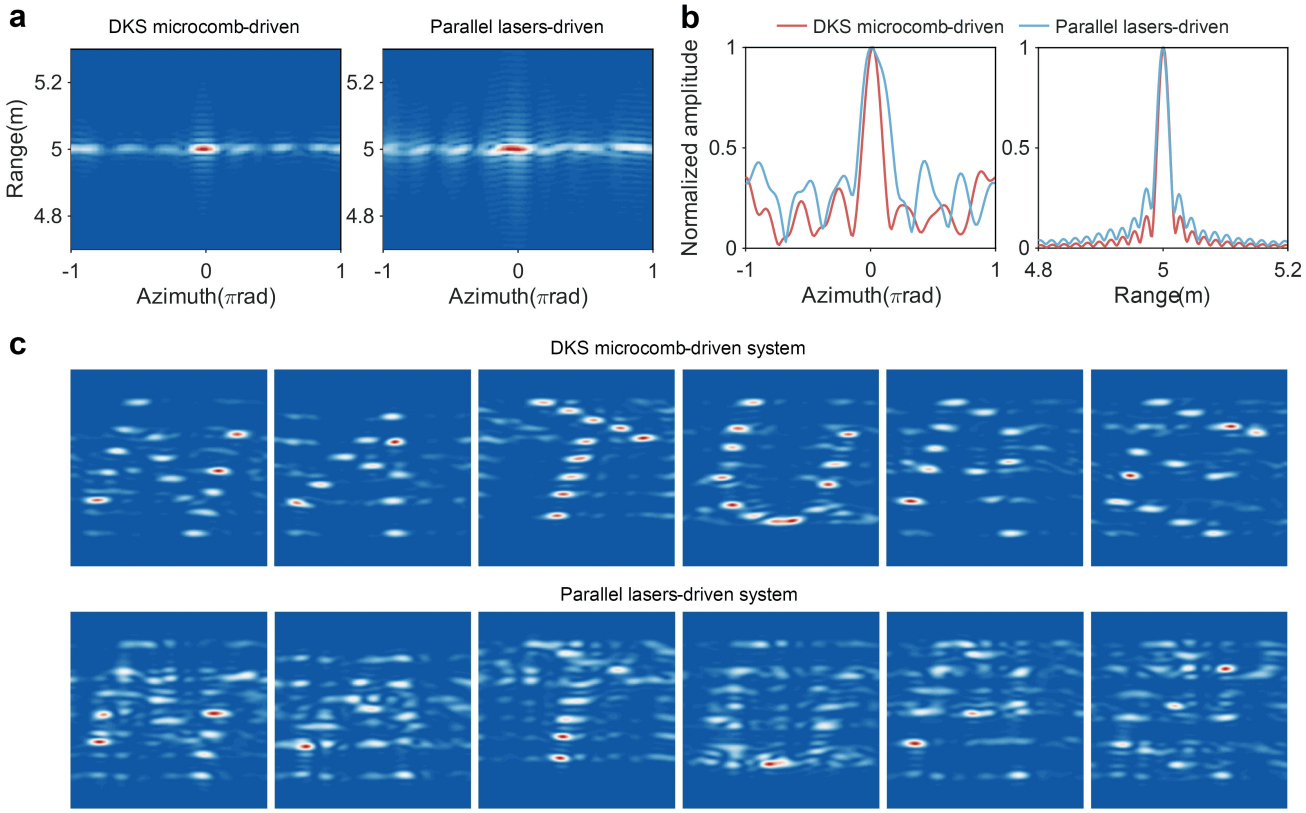


Figure 5. **Forward-looking imaging demonstration. a.** Comparative 2D imaging results of a single point target (range: 5 m, elevation: 5°, azimuth: 0). The microcomb-driven system (left) yields a tightly focused spot, while the parallel-laser system (right) shows significant coupling and distortion. **b.** Azimuth profiles (left). The microcomb-driven system reaches 0.185π (near the 0.134π theoretical limit), while the parallel-laser system resolves 0.276π due to mode aliasing. Range profiles (right). Both systems achieve $\approx$ 2.1 cm FWHM. The parallel-lasers case shows higher sidelobes. **c.** Imaging result of a complex target ("NATURE") using the microcomb-driven system (top), exhibiting clear legibility. The same scene imaged by the parallel-laser system (bottom), where the target is unrecognizable due to severe background noise and spurious artifacts.

system driven by free-running discrete parallel lasers. Details on the parallel lasers-driven system are introduced in Methods. As shown in Figure. 4b, this system, hampered by the stochastic relative phase jitter of independent optical carriers, produces severely distorted fields. The intensity profiles lose their circular symmetry, exhibiting irregular "hotspots," while the phase branches become indistinct and the near-axis phase loses its linear variation characteristic with the azimuth, particularly at higher OAM modes where phase sensitivity is acute. In the DKS microcomb–driven case, narrow optical linewidth and stable carrier phases suppress inter-channel phase error, yielding nearly azimuth-invariant ring-like radiation intensity and pure-state phase distribution.

The observed changes in amplitude and phase patterns are primarily attributed to variations in the OAM modes carried by the vortex EM wave. To quantify the mode content, we performed OAM spectral decomposition over l = -7…+7 at 18 GHz and 22 GHz with an elevation angle of 8° (Figure. 4c). In the microcomb-driven case, the spectra remain dominated by the intended OAM mode, with only minor sidelobes that can be attributed to finite aperture, spatial sampling and residual calibration error. In contrast, the parallel-laser baseline exhibits pronounced leakage into adjacent modes and, for higher OAM mode or lower frequency, a shift of the dominant spectral line away from the programmed value. This behavior is consistent with inter-channel phase jitter and amplitude non-uniformity, which perturb the designed phase distribution and introduce mode aliasing.

To provide a rigorous metric, we calculated the Fundamental-mode Energy Ratio (FER) and the Degree of Intensity Deviation (DID) [46] (see Supplementary Note 3 for mathematical definitions). Figure. 4d plots the FER versus elevation for l = 3 at 18 and 22 GHz, comparing theoretical predictions with experimental measurements from both the DKS microcomb and parallel-laser systems. At both frequencies, the microcomb-driven curves closely track the theoretical model, consistently maintaining high purity levels above the parallel-laser baseline across the full elevation range. This alignment confirms that the generated fields approach an ideal pure state. The DID results reinforce this conclusion (Figure. 4e). Across elevation angles and frequencies, the microcomb-driven system

maintains lower intensity deviation than the parallel-laser baseline, indicating closer agreement with the ideal mode profile. Meanwhile, combining the results in Figs. 4c and 4d indicates that mode purity is more susceptible to errors at elevation positions with weak radiation energy. Therefore, especially in microwave sensing applications such as forward-looking detection with small elevation angles, the potential of the proposed system to obtain high-performance results will be more prominent.

Resolution analysis and forward-looking imaging

The superior field quality and mode purity translate directly into enhanced vortex EM sensing performance. To validate this, we performed forward-looking imaging experiments using a multiple-input single-output (MISO) configuration, employing a two-dimensional FFT algorithm [47] to reconstruct targets from the collected echoes (details on the sensing model and imaging principle are introduced in Methods and Supplementary Note 4.).

We first evaluated the system's spatial resolution using a single point target positioned at a range of 5 m, an elevation angle of 5° and an azimuth of 0. The transmitter sequentially radiated 15 pulses carrying OAM modes l = -7...+7, each using a linear frequency sweep from 18 to 26 GHz with a 200 kHz step size (8 GHz span). Figure. 5a presents the comparative 2D imaging results. The microcomb-driven system yields a tightly focused, high-contrast reconstruction with a clean background. In contrast, due to the low OAM mode purity, the parallel-laser baseline exhibits significant coupling between the azimuth and range axes, resulting in a broadened and distorted target response. These will cause mutual influence between scatters, leading to aliasing of target information, making it difficult to extract and analyse its features.

To analyse the achievable resolution of the proposed system, the range and azimuth profiles are compared in Figure. 5b. In range direction, both systems achieve the full width at half maximum (FWHM) $\approx$ 2.1 cm, close to the theoretical limit of 1.875 cm (dictated by the 8 GHz bandwidth). However, the parallel lasers-driven curve shows higher sidelobe level due to range-azimuth coupling introduced by degraded OAM purity. In azimuth direction, the angular resolution of DKS microcomb-driven system is measured to be 0.185π, proximate to the theoretical value of 0.134π (determined by the aperture of 15 OAM modes). In contrast, the parallel lasers-driven system, affected by OAM mode aliasing, demonstrated an actual angular resolution of only 0.276π, which is twice as poor as the theoretical resolution.

We further evaluated the ability of the system to resolve a more complex target by imaging a "*NATURE*" shaped target composed of six groups of point scatterers forming the letters "*N*", "*A*", "*T*", "*U*", "*R*", and "*E*" (Figure. 5c). The microcomb-driven system successfully reconstructs each letter with sharp boundaries and negligible background artifacts. The spatial separation between individual scatterers is clearly resolved. Conversely, with the conventional parallel lasers-driven system, only coarse target locations are recovered. Strong sidelobes cause overlap among point responses, hindering correct focusing and introducing spurious targets. These experiments demonstrate that high-purity, multimode broadband vortex EM waves yield distinct advantages in terms of sharp focusing, suppressed sidelobes, and superior azimuth discrimination, establishing the proposed architecture as a robust platform for high-performance microwave sensing applications.

Discussion

We have demonstrated an integrated microwave photonic architecture that synthesizes high-purity, broadband vortex EM waves for high-resolution forward-looking sensing. The core advancement lies in the system-level synergy between photonic integration and microwave photonic processing. By harnessing a single DKS microcomb, we provide a naturally coherent and dense grid of optical carriers, eliminating the stochastic phase noise and hardware complexity inherent to current systems. Meanwhile, performing phase and amplitude control in the optical domain, ensures flat amplitude and phase responses across the entire RF bandwidth, a capability difficult to achieve with electronic beamformers. Our measurements show that, relative to a free-running parallel-laser implementation, the microcomb-driven system exhibits improved field integrity and higher OAM-mode purity. These improvements are consistent with the sharper focusing, reduced sidelobes, and clearer image reconstruction observed in the forward-looking imaging experiments.

While the current system exhibits superior performance, a rigorous analysis of the source characteristics reveals potential avenues for further optimization. Although the effective linewidths of the generated comb lines (<12 kHz) are orders of magnitude narrower than typical semiconductor laser arrays, they are not uniform across the spectrum. As observed in our measurements, the linewidths exhibit a parabolic degradation as the frequency offset from the pump increases due to TRN. However, our analysis confirms that even for the outermost channels, the effective coherence length remains orders of magnitude larger than the maximum path delay variations in our imaging setup. Consequently, the purity of the high-order OAM modes (e.g., $l = 7$) is preserved, as evidenced by the high FER measurements in Figure. 4. While not prohibitive for current demonstrations, this effect could impose a practical limit on the number of usable channels for ultra-high-purity applications. Future iterations could mitigate this through active suppression techniques, such as Pound–Drever–Hall (PDH) locking or auxiliary laser cooling, alongside cavity dispersion engineering to flatten the local dispersion profile.

Looking beyond the current architecture, the ultimate trajectory of this technology is the realization of a fully monolithic system-on-chip. In our current demonstration, the external fiber pump laser and the programmable optical signal processor remain as discrete components. To address the source integration, leveraging stimulated Brillouin scattering (SBS) in high-Q microcavities offers a route to "self-pumped" soliton generation. Recent advances have shown that backward Brillouin scattering in a micro-disk resonator can initiate Brillouin-Kerr solitons, potentially obviating the need for an external narrow-linewidth pump laser [48, 49]. While such suspended micro-disk structures currently pose fabrication challenges compared to the robust CMOS-compatible architecture used here, offer an intriguing path towards even narrower linewidths and the removal of the external pump laser [50]. Simultaneously, to eliminate the discrete optical waveshaper, future work will focus on on-chip signal processing strategies. By incorporating integrated optical delay networks or reconfigurable mesh architectures directly onto the photonic chip, and coupling them with advanced vortex EM detection models [51], we can replace the bulky commercial processor. This evolution would not only drastically reduce the form factor but also enhance reconfigurability and processing speed, paving the way for handheld or on-chip sensor nodes.

In conclusion, we have realized a high-performance, integrated vortex EM sensing system powered by a soliton microcomb. It directly addresses longstanding barriers in coherent multi-channel wavefront synthesis. By providing a scalable path to broadband, high-purity OAM generation in a compact form factor, our platform opens new opportunities for high-resolution radar and a new generation of integrated smart sensors. Although this work primarily validated the system for forward-looking imaging, the underlying capability to generate high-fidelity, multi-mode waveforms is broadly applicable. It holds significant potential for diverse microwave sensing scenarios where compact size, high resolution, and operation without platform motion are paramount. This integration of nonlinear photonics, chip-scale optics, and microwave engineering marks a decisive step toward deployable, high-performance smart sensors.

Methods

Linewidth measurement. The effective linewidths of the Kerr-comb lines were measured using the delayed self-heterodyne method [36]. A target comb line was first isolated using a tunable optical filter, amplified by an EDFA, and filtered again to suppress amplified spontaneous emission noise. The filtered comb line was subsequently split into two paths via a 3-dB coupler. One path passed through an acousto-optic modulator (AOM) that imposed an 80-MHz frequency shift, followed by approximately 10 km of single-mode fiber to induce decoherence delay. The delayed and undelayed paths were recombined and detected by a balanced photodetector, generating a non-zero-frequency delayed self-heterodyne signal centered at 80 MHz. The beat spectrum was analyzed using an electrical spectrum analyzer (ESA). The effective linewidth was obtained by fitting the beat note with a Lorentzian profile and dividing the extracted 3-dB full width at half maximum by two. The reference benchtop laser was characterized using the identical procedure for valid comparison.

Broadband signal synthesis and optical control. The modulated soliton comb was amplified and directed to a programmable optical signal processor (Waveshaper 16000A, Finisar), which is programmable to any combination of attenuation and phase profiles with a high spectral resolution over the input optical spectrum. Sixteen channels were selected from the modulated DKS comb, with carrier wavelengths of $\lambda_1 = 1553.21$ nm, $\lambda_2 = 1553.98$ nm, $\lambda_3 = 1554.76$ nm, $\lambda_4 = 1555.53$ nm, $\lambda_5 = 1556.30$ nm, $\lambda_6 = 1557.08$ nm, $\lambda_7 = 1557.85$ nm, $\lambda_8 = 1558.63$ nm, $\lambda_9 = 1559.40$ nm, $\lambda_{10} = 1560.18$ nm, $\lambda_{11} = 1560.95$ nm, $\lambda_{12} = 1561.73$ nm, $\lambda_{13} = 1562.52$ nm, $\lambda_{14} = 1563.30$ nm, $\lambda_{15} = 1564.08$ nm, and $\lambda_{16} = 1564.86$ nm. In the nth output channel, the optical carrier at λ_n and its $+1^{st}$ order modulation sideband were retained, and a phase shift of $\varphi_n = 2\pi ln/N$ was imposed between them. The processed signals were converted to the electrical domain by a photodetector array. The generated electrical signal in the nth channel can be expressed as

$$I_{\mathrm{PD}n}(t) \propto (1 + \delta A_{n\mathrm{intra}} + \delta A_{n\mathrm{inter}}) \cdot \cos\left(2\omega_{RF}t + \varphi_n + \delta\varphi_{n\mathrm{intra}} + \delta\varphi_{n\mathrm{inter}}\right) \quad (1)$$

where ω_{RF} is the angular frequency of the RF signal. The terms $\delta A_{n\ \mathrm{intra}}$ and $\delta A_{n\ \mathrm{inter}}$ represent the intra-channel and inter-channel amplitude fluctuations, respectively, while $\delta\varphi_{n\ \mathrm{intra}}$ and $\delta\varphi_{n\ \mathrm{inter}}$ denote the corresponding intra-channel and inter-channel phase errors. The rigorous suppression of these error terms is central to the high-performance imaging demonstrated in this work (see Supplementary Note 5). After photodetection, the resulting RF signals were radiated by the UCA to synthesize the vortex EM wave. By adjusting the parameter settings of the waveshaper, the OAM mode carried by the synthesized EM wave can be flexibly changed. The maximum achievable OAM mode l_{max} is limited by the number of spatial sampling points in the array (i.e., following the Nyquist sampling criterion, $l_{max} < N/2$).

For the comparative baseline, we employed four multi-channel laser sources (two Agilent N7714A units and two ID Photonics CoBriteDX4 units) to provide 16 optical carriers with wavelengths of $\lambda_1 = 1554.8$ nm, $\lambda_2 = 1555.5$ nm, $\lambda_3 = 1556.3$ nm, $\lambda_4 = 1557.0$ nm, $\lambda_5 = 1557.7$ nm, $\lambda_6 = 1558.4$ nm, $\lambda_7 = 1559.2$ nm, $\lambda_8 = 1559.9$ nm, $\lambda_9 = 1560.6$ nm, $\lambda_{10} = 1561.3$ nm, $\lambda_{11} = 1562.1$ nm, $\lambda_{12} = 1562.8$ nm, $\lambda_{13} = 1563.5$nm, $\lambda_{14} = 1564.2$ nm, $\lambda_{15} = 1565.0$ nm, and $\lambda_{16} = 1565.7$ nm. Unlike the microcomb, these carriers exhibit non-uniform spacing and independent phase drifts. These carriers were combined via a commercial wavelength division multiplexer (WDM) and then passed through

the same modulation, optical processing, photodetection and radiation chain used in the microcomb-driven implementation.

Vortex EM imaging and reconstruction algorithm. We employed a MISO scheme [52, 53] for forward-looking vortex EM imaging. Radar echoes were collected by a single receive antenna. The collected data was arranged as a two-dimensional matrix $S(l,k)$ over the OAM-mode index and frequency. In vortex EM sensing, the OAM index l is approximately dual to the target azimuth ϕ. Conventional reconstruction applies a 2-D Fourier transform across frequency domain (to range) and across the OAM-mode domain (to azimuth). However, unlike multi-input multi-output (MIMO) scheme, the MISO configuration introduces a single Bessel factor (rather than squared factor $J_l^2(.)$). This introduces an l-dependent π-phase flip in the echo envelope and yields an azimuth point-spread function (PSF) exhibiting two symmetric peaks around $\pm\pi/2$ with no dominant DC component after the OAM-mode domain transform, which degrades azimuth focusing. To remove this ambiguity, we implemented a mode-wise phase compensation prior to imaging. For any mode where $J_l\left(ka\sin\theta_{\mathrm{ref}}\right)<0$ (θ_{ref} is the nominal elevation of the region of interest, typically the scene center), the corresponding echo data was multiplied by -1, canceling the hidden phase jump. After compensation, the azimuth PSF collapses to a single main lobe centered at zero spatial frequency, restoring unambiguous azimuth discrimination. The range resolution is determined by the bandwidth of vortex EM waves, $\Delta r=\mathrm{c}/(2B)$. The azimuth resolution is governed by the number of utilized OAM modes l_{num}, $\Delta\phi=2\pi/l_{num}$.

Data Availability: The data that support the findings of this study are available from the corresponding authors upon reasonable request.

Code Availability: The codes that support the findings of this study are available from the corresponding authors upon reasonable request.

Contributions: S.L.P. and Y.P.W. suggested the designs, planned, and supervised the work. G.Q.S., and Z.K.Z. conceived the idea, carried out the analytical modeling and numerical simulations. G.Q.S., Z.K.Z., J.C.G., W.J.Q., D.C., and H.Z. built the system and performed the experimental measurements. G.Q.S., Z.K.Z, and H.Z. performed the data analysis. S.L.P., Y.P.W., F.Z.Z., J.J.H., G.Q.S., Z.K.Z., and H.Z. wrote the manuscript. All authors discussed the theoretical aspects and numerical simulations, interpreted the results, and reviewed the manuscript.

Acknowledgements: This work is supported in part by the National Natural Science Foundation of China (62571238, 62271249, 62371224); the Natural Science Foundation of Jiangsu Province (BK20232033); the Leading-Edge Technology Program of Jiangsu Natural Science Foundation (BK20232001); the Key Laboratory of Radar Imaging and Microwave Photonics (NUAA), Ministry of Education, under Grant (NJ20250001); the Fundamental Research Funds for the Central Universities (B250201253).

References

[1] Nanzer, J. A., A review of microwave wireless techniques for human presence detection and classification, *IEEE Trans. Microw. Theory Techn.* **65**, 1780–1794 (2017).

[2] Brinker, K., Dvorsky, M., Al Qaseer, M. T. & Zoughi, R., Review of advances in microwave and millimetre-wave NDT&E: principles and applications, *Phil. Trans. R. Soc. A* **378**, 20190585 (2020).

[3] Mavrovic, A. et al., Reviews and syntheses: recent advances in microwave remote sensing in support of terrestrial carbon cycle science in Arctic–boreal regions, *Biogeosciences.* **20**, 2941–2970 (2023).

[4] Chen, C. C. & Andrews, H. C., Target-motion-induced radar imaging, *IEEE Trans. Aerosp. Electron. Syst.* **AES-16**, 2–14 (1980).

[5] Wahl, D. E., Eichel, P. H., Ghiglla, D. C. & Jakowatz, C. V., Phase gradient autofocus—a robust tool for high resolution SAR phase correction, *IEEE Trans. Aerosp. Electron. Syst.* **30**, 827–835 (1994).

[6] Bamler, R., A comparison of range-Doppler and wavenumber domain SAR focusing algorithms, *IEEE Trans. Geosci. Remote Sens.* **30**, 706–713 (1992).

[7] Zheng, Y., Tseng, S.-M. & Yu, K.-B., Closed-form four-channel monopulse two-target resolution, *IEEE Trans. Aerosp. Electron. Syst.* **39**, 1083–1089 (2003).

[8] Prost, R. & Goutte, R., Discrete constrained iterative deconvolution algorithms with optimized rate of convergence, *Signal Process.* **7**, 209–230 (1984).

[9] Chen, R., Zhou, H., Moretti, M., Wang, X. & Li, J., Orbital angular momentum waves: generation, detection and emerging applications, *IEEE Commun. Surv. Tut.* **22**, 840–868 (2020).

[10] Liu, K., Cheng, Y., Li, X. & Gao, Y., Microwave-sensing technology using orbital angular momentum: overview of its advantages, *IEEE Veh. Technol. Mag.* **14**, 112–118 (2019).

[11] Li, L. & Li, F., Beating the Rayleigh limit: orbital-angular-momentum-based super-resolution diffraction tomography, *Phys. Rev. E* **88**, 033205 (2013).

[12] Allen, L., Beijersbergen, M. W., Spreeuw, R. J. C. & Woerdman, J. P., Orbital angular momentum of light and the transformation of Laguerre–Gaussian laser modes, *Phys. Rev. A* **45**, 8185–8189 (1992).

[13] Lavery, M. P. J. et al., Detection of a spinning object using light's orbital angular momentum,

Science **341**, 537–540 (2013).

[14] Yang, T. L., Li, S., Xu, O., Li, W. & Wang, Y., Three dimensional SAR imaging based on vortex electromagnetic waves, *Remote Sens. Lett.* **9**, 343–352 (2018).

[15] Zhang, W. H. et al., Free-space remote sensing of rotation at the photon-counting level, *Phys. Rev. Appl.* **10**, 044014 (2018).

[16] Song, X. et al., Full dimensional control of structured microwaves based on microcombs, *Nat. Photon.* **20**, 1–9 (2026).

[17] Zou, K., Zhu, Y., Zhang, F. & Chen, Z., Spectrally efficient terabit optical transmission with Nyquist 64-QAM half-cycle subcarrier modulation and direct detection, *Opt. Lett.* **41**, 2767–2770 (2016).

[18] Zhang, W. et al., Quantum remote sensing of the angular rotation of structured objects, *Phys. Rev. A* **100**, 043832 (2019).

[19] Gao, X. et al., Generating the orbital angular momentum of radio frequency signals using optical-true-time-delay unit based on optical spectrum processor, *Opt. Lett.* **39**, 2652–2655 (2014).

[20] Sun, G., Zhang, F., Zhao, K. & Pan, S., Photonics-based broadband vortex electromagnetic wave generation for high-resolution imaging, *J. Lightw. Technol.* **42**, 1894–1900 (2024).

[21] Strain, M. J. et al., Fast electrical switching of orbital angular momentum modes using ultracompact integrated vortex emitters, *Nat. Commun.* **5**, 4856 (2014).

[22] Zhang, J. et al., An InP-based vortex beam emitter with monolithically integrated laser, *Nat. Commun.* **9**, 2652 (2018).

[23] Chen, B. et al., Integrated optical vortex microcomb, *Nat. Photon.* **18**, 625–631 (2024).

[24] Liu, Y. et al., Integrated vortex soliton microcombs, *Nat. Photon.* **18**, 632–637 (2024).

[25] Chang, L., Liu, S. & Bowers, J. E., Integrated optical frequency comb technologies, *Nat. Photon.* **16**, 95–108 (2022).

[26] Guo, J. et al., Chip-based laser with 1-hertz integrated linewidth, *Sci. Adv.* **8**, eabp9006 (2022).

[27] Isichenko, A. et al., Sub-Hz fundamental, sub-kHz integral linewidth self-injection locked 780 nm hybrid integrated laser, *Sci. Rep.* **14**, 27015 (2024).

[28] Metcalf, A. J. et al., High-power broadly tunable electrooptic frequency comb generator, *IEEE J. Sel. Top. Quantum Electron.* **19**, 231–236 (2013).

[29] Beha, K. et al., Electronic synthesis of light, *Optica* **4**, 406–411 (2017).

[30] Yu, F., Miao, R., Yin, K. et al., Broadband EO-comb generation based on two-stage nonlinear system, *IEEE Photon. J.* **14**, 1–5 (2022).

[31] Zhang, M. et al., Broadband electro-optic frequency comb generation in a lithium niobate microring resonator, *Nature* **568**, 373-377 (2019).

[32] Kippenberg, T. J., Gaeta, A. L., Lipson, M. & Gorodetsky, M. L., Dissipative Kerr solitons in optical microresonators, *Science* **361**, eaan8083 (2018).

[33] Nishimoto, K., Minoshima, K., Yasui, T. & Kuse, N., Investigation of the phase noise of a microresonator soliton comb, *Opt. Express* **28**, 19295–19303 (2020).

[34] Lei, F. et al., Optical linewidth of soliton microcombs, *Nat. Commun.* **13**, 1–9 (2022).

[35] Yang, H. et al., 5.2-THz-bandwidth miniaturized spectrometer using a GHz-tunable laser, *PhotoniX* **6**, 32 (2025).

[36] Huang, G. et al., Thermorefractive noise in silicon-nitride microresonators, *Phys. Rev. A* **99**, 061801 (2019).

[37] Lucas, E. et al., Ultralow-noise photonic microwave synthesis using a soliton microcomb-based transfer oscillator, *Nat. Commun.* **11**, 374 (2020).

[38] Drake, T. E., Stone, J. R., Briles, T. C. & Papp, S. B., Thermal decoherence and laser cooling of Kerr microresonator solitons, *Nat. Photon.* **14**, 480–485 (2020).

[39] Stone, J. R. & Papp, S. B., Harnessing dispersion in soliton microcombs to mitigate thermal noise, *Phys. Rev. Lett.* **125**, 153901 (2020).

[40] Ye, Z. et al., Foundry manufacturing of tight-confinement, dispersion-engineered, ultralow-loss silicon nitride photonic integrated circuits, *Photonics Res.* **11**, 558 (2023).

[41] Luo, Y. H. et al., A wideband, high-resolution vector spectrum analyzer for integrated photonics, *Light.: Sci. Appl.* **13**, 83 (2024).

[42] Chen, D. et al., Light coupling to photonic integrated circuits using optimized lensed fibers, *Phys. Rev. Appl.* **25**, 014078 (2026).

[43] Wang, W., Wang, L. & Zhang, W., Advances in soliton microcomb generation, *Adv. Photon.* **2**,

034001 (2020).

[44] Guo, H., Karpov, M., Lucas, E. et al., Universal dynamics and deterministic switching of dissipative Kerr solitons in optical microresonators, *Nat. Phys.* **13**, 94–102 (2017).

[45] Lu, Z. et al., Deterministic generation and switching of dissipative Kerr soliton in a thermally controlled micro-resonator, *AIP Adv.* **9**, 025314 (2019).

[46] Yuan, T., Cheng, Y., Wang, H. & Qin, Y., Mode characteristics of vortical radio wave generated by circular phased array: theoretical and experimental results, *IEEE Trans. Antennas Propag.* **65**, 688–695 (2017).

[47] Liu, K., Cheng, Y., Gao, Y., Li, X., Qin, Y. & Wang, H., Super-resolution radar imaging based on experimental OAM beams, *Appl. Phys. Lett.* **110**, 164102 (2017).

[48] Bai, Y. et al., Brillouin-Kerr soliton frequency combs in an optical microresonator, *Phys. Rev. Lett.* **126**, 063901 (2021).

[49] Zhang, M. et al., Strong interactions between solitons and background light in Brillouin-Kerr microcombs, *Nat. Commun.* **15**, 1661 (2024).

[50] Xia, D. et al., Reconfigurable chalcogenide integrated nonlinear photonics, *Nat. Commun.* **16**, 10133 (2025).

[51] Sun, G., Zhang, F. & Pan, S., Frequency-dependent vortex electromagnetic wave imaging, *IEEE Antennas Wirel. Propag. Lett.* **24**, 23–27 (2025).

[52] Yuan, T., Wang, H., Cheng, Y. et al., Electromagnetic vortex-based radar imaging using a single receiving antenna: theory and experimental results, *Sensors* **17**, 630 (2017).

[53] Qu, H., Li, S., Chen, C. et al., High-resolution orbital angular momentum imaging with the removal of Bessel function modulation effect, *IEEE Trans. Microw. Theory Techn.* **72**, 2577–2590 (2023).

Supplementary Files

This is a list of supplementary files associated with this preprint. Click to download.

- SupplementaryInformation.pdf